

# Chapter 2

## Scanning Tunneling Spectroscopies of Magnetic Atoms, Clusters, and Molecules



Jörg Kröger, Alexander Weismann, Richard Berndt, Simon Altenburg, Thomas Knaak, Manuel Gruber, Andreas Burtzloff, Nicolas Néel, Johannes Schöneberg, Laurent Limot, Takashi Uchihashi and Jianwei Zhang

**Abstract** The Kondo effect of adatoms on surfaces may to some extent be controlled by manipulating their electronic and geometric environment. Results are presented from artificial structures like quantum well systems, from arrangements of single atoms made with a scanning tunneling microscope, and from custom-made molecules. Spin-orbit coupling at single adatoms is probed via measurements of the anisotropic magnetoresistance, in particular in single atom contacts. Such junctions are also investigated with respect to the current shot noise, which is influenced by the electron spin.

The Kondo effect is one of the key correlation effects in condensed matter physics. Originally it was observed as an increase of the resistivity of metals with dilute magnetic impurities below a characteristic temperature [1]. Kondo explained these observations in terms of conduction electron scattering off the impurity magnetic moment [2]. The scattering processes involve spin flips of the conduction electrons and of the magnetic impurity, which leads to an efficient screening of the magnetic moment. The spectroscopic signature of the resulting many-body nonmagnetic

---

J. Kröger · N. Néel  
Institut für Physik, Technische Universität Ilmenau, 98684 Ilmenau, Germany

A. Weismann · R. Berndt (✉) · T. Knaak · M. Gruber · A. Burtzloff · J. Schöneberg  
J. Zhang  
Institut für Experimentelle und Angewandte Physik, Christian-Albrechts-Universität zu Kiel,  
24098 Kiel, Germany  
e-mail: berndt@physik.uni-kiel.de

S. Altenburg  
Bundesanstalt für Materialforschung und -prüfung, 12205 Berlin, Germany

L. Limot  
Université de Strasbourg, CNRS, IPCMS, UMR 7504, F-67000 Strasbourg, France

T. Uchihashi  
International Center for Materials Nanoarchitectonics, National Institute  
for Materials Science, 1-1, Namiki, Tsukuba, Ibaraki 305-0044, Japan

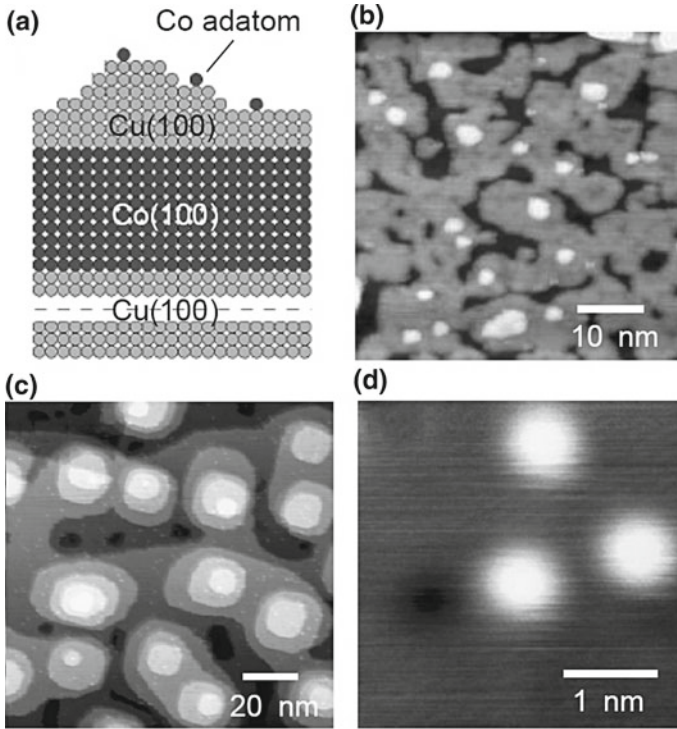
singlet ground state is the Abrikosov-Suhl [3–5] or Kondo resonance at the Fermi energy,  $E_F$  [6, 7]. The resonance width reflects the Kondo energy scale,  $k_B T_K$  ( $k_B$ : Boltzmann constant,  $T_K$ : Kondo temperature), where  $T_K$  is characteristic of the magnetic impurity and the substrate host. Since the first observation of the Kondo effect in scanning tunneling microscope (STM) experiments [8, 9] a wealth of scanning tunneling spectroscopy (STS) data has been published for a variety of adatoms on metal surfaces [10].

Here we focus on experiments that aim at controlling the Kondo effect of adatoms by manipulating their electronic and geometric environment. A number of approaches have been used so far. Electronic quantum well states affect the electronic density of states but have little impact on the adsorption geometry of an adatom. In Sect. 2.1.1 we show that they effectively modulate the Kondo temperature  $T_K$  of Co atoms. The addition of adatoms to a magnetic impurity also modifies  $T_K$  as demonstrated by experiments on heterogeneous clusters comprised of Co and non-magnetic Cu atoms (Sect. 2.1.2). Chains of Cu atoms may also be used to mediate interactions between two Co atoms (Sect. 2.1.3). Next, the apex atom of an STM tip may be brought closer to a magnetic impurity to controllably increase the interaction with an additional neighbor atom (Sect. 2.1.4). Natural extensions of the approach outlined so far are to use organic molecules to obtain interconnected magnetic impurities (Sect. 2.2) or to tune the substrate-impurity interaction by an interlayer of graphene (Sect. 2.3). The role of spin-orbit coupling (SOC) in transport phenomena is another research frontier in spintronics [11–16]. One of its intriguing consequences is the occurrence of anisotropic magnetoresistance (AMR). Section 2.4 focuses on AMR in single-atom contacts, for which particularly large effects have been predicted. Finally, Sect. 2.5 presents measurements of the current shot noise in single atom junctions. Electron correlation tends to reduce the shot noise and noise data consequently are an additional tool to investigate spin physics in nanoscale junctions.

## 2.1 Tuning the Kondo Effect on the Single-Atom Scale

### 2.1.1 Co Atoms on a Quantum Well System

A model system was used for tuning the Kondo temperature by the local density of states (LDOS) at  $E_F$  [17]. Co atoms adsorbed on layers of Cu and Co on a Cu(100) substrate [Fig. 2.1a] were investigated by spectroscopy of the differential conductance ( $dI/dV$ ). An excellent lattice match enables epitaxial growth of face-centered cubic Co(100) on Cu(100) [Fig. 2.1b] and subsequently of Cu(100) on Co(100) [Fig. 2.1c]. This layered system is an ideal platform for acquiring spectra of single Co atoms on Cu layers [Fig. 2.1d] of various thicknesses without changing the imaging area. The local thickness of Cu layers ( $d_{Cu}$ ) was determined from the energies of quantum well states (QWS) vertically confined to the Cu layers by reflection at the vacuum–Cu and Cu–Co interfaces [18–24].



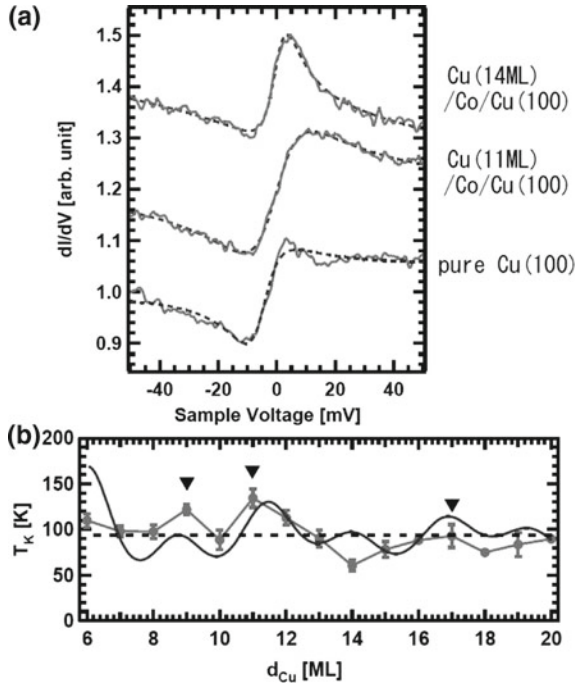
**Fig. 2.1** **a** Sketch of Cu/Co/Cu(100) multilayer with adsorbed single Co atoms. STM images of **b** a 10-ML-thick Co overlayer grown on a Cu(100) substrate (current  $I = 100$  pA, bias voltage  $V = 200$  mV), **c** a 15-ML-thick Cu overlayer grown on a Co/Cu(100) multilayer (100 pA, 200 mV), and **d** of Co atoms deposited on a Cu/Co/Cu(100) multilayer (100 pA, 300 mV). Reprinted with permission from T. Uchihashi et al., Phys. Rev. B **78**, 033402 (2008) [17]. Copyright 2008 by the American Physical Society

Figure 2.2a shows  $dI/dV$  spectra of Co atoms on a pristine Cu(100) surface (bottom) and on Cu layers above Co(100) on Cu(100) with thicknesses of 11 (middle) and 14 monolayers (top). The Kondo resonance of Co leads to characteristic asymmetric features around zero bias voltage. In STS the Kondo resonance generally appears with a Fano line shape, which may adopt diplike, peaklike or asymmetric profiles [25, 26]. To quantitatively analyze the  $dI/dV$  data, the experimental spectra were fit by

$$\frac{dI}{dV} = af(V) + b + cV \quad (2.1)$$

with

$$f(V) = \frac{[q + \varepsilon(V)]^2}{1 + \varepsilon(V)^2} \quad (2.2)$$



**Fig. 2.2** **a**  $dI/dV$  spectra measured above Co atoms on Cu/Co/Cu(100) multilayers. Top: 14 ML Cu. Middle: 11 ML Cu. Bottom: bare Cu(100). Spectra are offset for clarity. Fits according to (2.1) are shown as dashed lines. **b** Mean Kondo temperature  $T_K$  of Co atoms on Cu/Co/Cu(100) multilayers versus Cu overlayer thickness  $d_{Cu}$  (circles). Half the error bar indicates the standard error of  $T_K$  for each  $d_{Cu}$ . A solid line shows calculated  $T_K$  values. The used fit parameters are  $A_b = 0.046 \text{ eV}^{-1} \text{ ML}$ ,  $\Phi_b = 0.26\pi$ ,  $A_n = 0.011 \text{ eV}^{-1} \text{ ML}$ ,  $\Phi_n = -0.03\pi$ . A dotted line indicates the mean  $T_K = 94 \text{ K}$  of Co atoms on pure Cu(100). Reprinted with permission from T. Uchihashi et al., Phys. Rev. B **78**, 033402 (2008) [17]. Copyright 2008 by the American Physical Society

the Fano function,  $\varepsilon(V) = (eV - \varepsilon_K)/(k_B T_K)$  ( $e$ : elementary charge,  $\varepsilon_K$ : resonance shift from  $E_F$ ),  $q$  the asymmetry parameter of the Fano theory,  $a$  the resonance amplitude, and  $b + cV$  a linear background. For the spectra shown in Fig. 2.2a the extracted Kondo temperatures are  $T_K = 67 \text{ K}$  (14 monolayers) and  $T_K = 139 \text{ K}$  (11 monolayers), which significantly deviate from  $T_{K,0} = 94 \pm 5 \text{ K}$  for Co on clean Cu(100) [27, 28]. Figure 2.2b shows  $T_K$  for Co atoms adsorbed on Cu layers with all investigated thicknesses. The obvious modulation of  $T_K$  with  $d_{Cu}$  reflects the variation of the LDOS at  $E_F$ ,  $\varrho_F$ , caused by the QWS confined to the Cu slab. Using

$$T_K = T_0 \exp\left(-\frac{1}{2\varrho_F J}\right) \quad (2.3)$$

with  $T_0$  a prefactor,  $J$  the exchange coupling constant between conduction electrons and impurity states together with

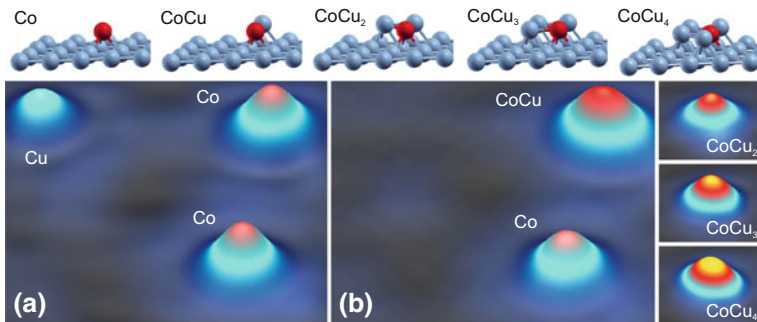


**Fig. 2.3** Top: Ball-and-stick models of fully relaxed adsorption structures of  $\text{CoCu}_n$  ( $0 \leq n \leq 4$ ) on  $\text{Cu}(111)$ . **a** STM constant current topograph of Cu and Co atoms on  $\text{Cu}(111)$  prior to the fabrication of  $\text{CoCu}_n$  clusters. **b** STM topographs showing different  $\text{CoCu}_n$  clusters. Images were acquired with  $V = 100$  mV and  $I = 0.1$  nA. Reprinted with permission from N. Néel et al., Phys. Rev. Lett. **101**, 266803 (2008) [32]. Copyright 2008 by the American Physical Society

$$\varrho_F = \varrho_{F,0} + \sum_{i=b,n} \frac{A_i}{d_{\text{Cu}}} \cos\left(\frac{2\pi d_{\text{Cu}}}{\Lambda_i} + \Phi_i\right) \quad (2.4)$$

$[A_i, \Lambda_i, \Phi_i$ : amplitude, spatial periodicity, phase of the quantum oscillation at the belly ( $i = b$ ) and the neck ( $i = n$ ) of the Cu Fermi surface] leads to a reasonable fit [full line in Fig. 2.2b] of the experimentally observed  $T_K$  variation. The fit was performed for fixed  $\Lambda_b = 5.88$  ML,  $\Lambda_n = 2.67$  ML [18, 21, 29], and free parameters  $A_i, \Phi_i$ . For Co on pristine  $\text{Cu}(100)$  the free-electron estimate  $\varrho_{F,0} = 0.11$  eV $^{-1}$  was used together with  $J \approx 1$  eV [25, 28, 30],  $T_K = 94$  K.

It is worth mentioning that the exchange interaction between a Co atom and the Co layer through the Cu layers,  $J_{\text{ex}}$ , is too weak to account for the observed changes in  $T_K$ . Indeed,  $J_{\text{ex}} = 1.5$  meV for  $d_{\text{Cu}} = 5$  ML [31] decreases rapidly with increasing  $d_{\text{Cu}}$ . Only for  $d_{\text{Cu}} \leq 4$  ML,  $J_{\text{ex}}$  was found to become comparable and larger than the Kondo energy scale,  $k_B T_K \approx 8$  meV. In summary, by changing  $\varrho_F$  through QWS confined to thin metal films the Kondo effect of single adsorbed atoms may be altered.

### 2.1.2 Kondo Effect in $\text{CoCu}_n$ Clusters

The key result of this section is the important role of the local and anisotropic electronic structure at the magnetic-impurity site for the Kondo effect [32]. The local environment of a Co atom on  $\text{Cu}(111)$  was modified by changing its coordination to successively attached Cu atoms. Sketches of the resulting  $\text{CoCu}_n$  ( $0 \leq n \leq 4$ ) clusters are shown in the top row of Fig. 2.3, accompanied by corresponding STM images in Fig. 2.3a, b.

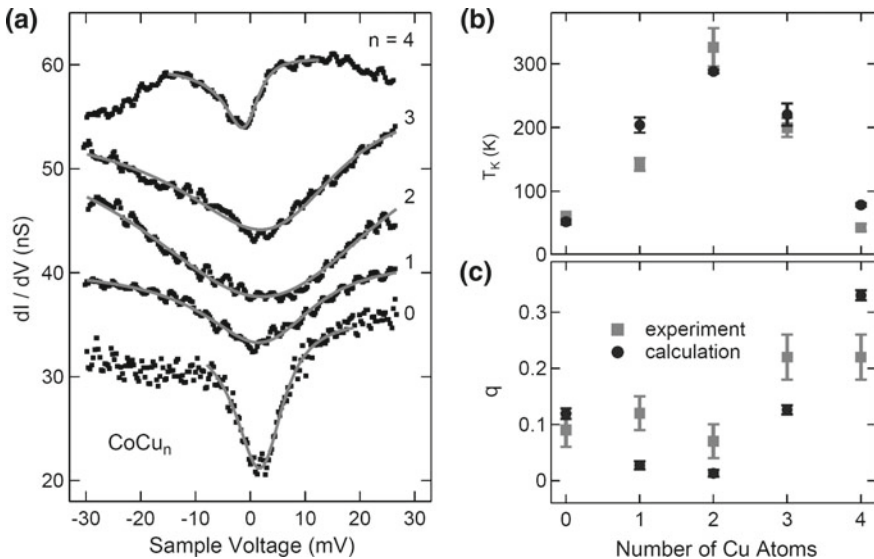


**Fig. 2.4** **a**  $dI/dV$  spectroscopy of  $\text{CoCu}_n$  clusters. The spectroscopic feature around zero bias is caused by the Kondo effect. Fano line shapes (2.1) were fit to the experimental data and are indicated as lines. Prior to spectroscopy tunneling parameters of  $V = 30$  mV and  $I = 1$  nA were used. Spectra with  $n = 1, \dots, 4$  are vertically offset by 5, 10, 20, 25 nS, respectively. Kondo temperatures (**b**) and line shape parameters (**c**) versus cluster size obtained from calculations (dots) and experiments (squares). Reprinted with permission from N. Néel et al., Phys. Rev. Lett. **101**, 266803 (2008) [32]. Copyright 2008 by the American Physical Society

Next,  $dI/dV$  spectra were acquired on top of single Co atoms and of  $\text{CoCu}_n$  clusters. A representative data set is shown in Fig. 2.4a. For the single Co atom the Kondo resonance appears as a sharp indentation around zero bias voltage. Upon adding Cu atoms, the  $dI/dV$  signature of the Kondo resonance strongly broadens and sharpens again after attaching a third and fourth Cu atom to Co. In contrast, the energies of the  $p_z$  states of the clusters decrease monotonically [32].

To see the changes clearly, the Kondo temperature and the asymmetry parameter were obtained by fitting (2.1) to  $dI/dV$  data and plotted as a function of the number of Cu atoms in Fig. 2.4b. The nonmonotonic behavior is readily visible. This peculiar variation of the Kondo resonance with the cluster size is at variance with the monotonic behavior of  $T_K$  with the average hybridization strength expected from bulk models of the Kondo effect.

Calculations of the local electronic structure of the  $\text{CoCu}_n$  clusters on Cu(111) reproduce the experimental data [32]. Calculated  $T_K$  and  $q$  are shown as dots in Fig. 2.4b and are summarized in Table 2.1 along with experimental data.  $T_K$  may be estimated as

$$T_K \approx W \sqrt{|\varrho_F J|} \exp\left(-\frac{1}{\varrho_F J}\right) \quad (2.5)$$

**Table 2.1** Experimental and calculated Kondo temperatures ( $T_K$ ) and line shape parameters ( $q$ ) of  $\text{CoCu}_n$  extracted from fits of Fano lines (2.1) to the spectra of Fig. 2.4a. Experimental uncertainty margins correspond to standard deviations obtained by a statistical analysis of a variety of fits. Calculated  $T_K$  and  $q$  are the arithmetic mean of values obtained by a Gaussian broadening of the  $sp$  LDOS by 100 meV and 50 meV. The uncertainty margins reflect the deviations of the arithmetic mean from data obtained using 100 meV and 50 meV broadening

| $n$ | Experiment   |                 | Calculation  |                 |
|-----|--------------|-----------------|--------------|-----------------|
|     | $T_K$ (K)    | $q$             | $T_K$ (K)    | $q$             |
| 0   | $61 \pm 4$   | $0.09 \pm 0.03$ | $52 \pm 4$   | $0.12 \pm 0.01$ |
| 1   | $142 \pm 10$ | $0.12 \pm 0.03$ | $204 \pm 12$ | $0.03 \pm 0.01$ |
| 2   | $326 \pm 30$ | $0.07 \pm 0.03$ | $288 \pm 3$  | $0.01 \pm 0.01$ |
| 3   | $200 \pm 15$ | $0.22 \pm 0.04$ | $221 \pm 18$ | $0.13 \pm 0.01$ |
| 4   | $43 \pm 6$   | $0.22 \pm 0.04$ | $79 \pm 3$   | $0.33 \pm 0.01$ |

( $W$ : width of the  $sp$  conduction band,  $J$ :  $sp$ - $d$  exchange interaction energy,  $\varrho_F$ : LDOS at  $E_F$  at the impurity site). Moreover, the asymmetry parameter reads

$$q = \frac{\gamma + \text{Re } G(E_F)}{\text{Im } G(E_F)} \quad (2.6)$$

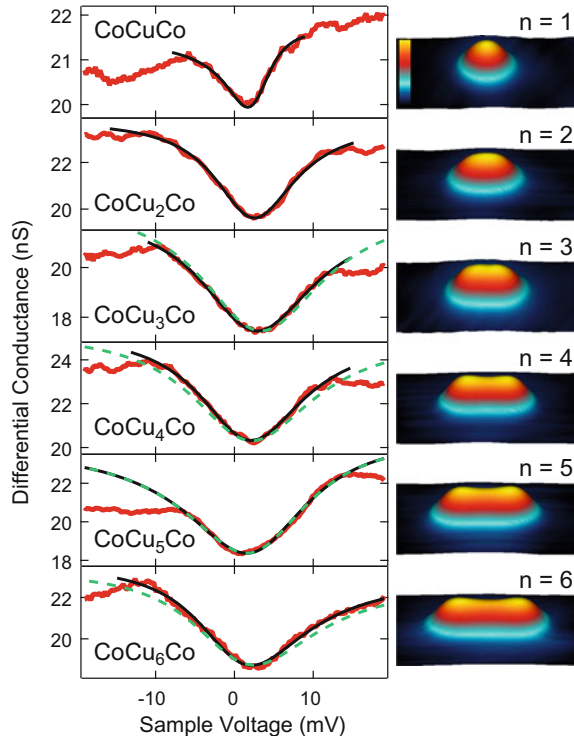
with  $G$  the local Green function of the conduction electrons.  $\gamma$  measures the ratio of the coupling of the STM tip to conduction electrons of the substrate and to localized Co  $d$  states [33]. Details of the calculations may be found elsewhere [32]. The simulations ( $W = 20$  eV,  $J = 1.3$  eV,  $\gamma = 0.22$  eV $^{-1}$ ) show that  $\varrho_F$  varies non-monotonically with the cluster size and thus leads to the variation of  $T_K$  and  $q$  observed in the experiments.

The evolution of  $\varrho_F$  can qualitatively be understood as follows. Co  $p$  orbitals have their main spectral weight above  $E_F$ , whereas  $s$  orbitals are mainly occupied. With increasing cluster size all orbitals shift to lower energies and the  $p$  ( $s$ ) orbital weight increases (decreases) at  $E_F$ . These variations do not perfectly cancel and thus lead to a nonmonotonic change of  $\varrho_F$ . In summary, atom-by-atom manipulation of the electronic structure at the Kondo impurity site induces a nonmonotonic variation of  $\varrho_F$ , the Kondo temperature, and the asymmetry factor. Simple scaling rules that predict a monotonous increase of  $T_K$  with the coordination number do not hold.

### 2.1.3 Two-Site Kondo Effect in Atomic Chains

Next, linear atomic chains are considered that host two Kondo atoms at their ends [34].  $\text{CoCu}_n\text{Co}$  ( $1 \leq n \leq 6$ ) clusters on Cu(111) are a model system for studying correlation effects. Local correlations are caused by Coulomb interaction at a particular site  $i$ . Nonlocal correlations are due to electrons propagating from site  $i$

**Fig. 2.5** **Left:**  $dI/dV$  spectra acquired above Co atoms of  $\text{CoCu}_n\text{Co}$  chains (red dots). Solid lines indicate Fano line shapes fit to the experimental data. The dashed lines are Fano lines for  $T_K = 110$  K, which correspond to a Co adatom attached to a  $\text{Cu}_4$  chain. **Right:** Pseudo-three-dimensional representations of STM topographs ( $38 \text{ \AA} \times 21 \text{ \AA}$ ) of linear  $\text{CoCu}_n\text{Co}$  clusters ( $n = 1 \dots 6$ ). Reprinted with permission from N. Néel et al., Phys. Rev. Lett. **107**, 106804 (2011) [34]. Copyright 2011 by the American Physical Society



to another site  $j$  with Coulomb scattering at both sites. Therefore, the Ruderman-Kittel-Kasuya-Yosida (RKKY) interaction [35–37] can cause magnetic correlations between distant atoms. When a Kondo effect is involved, the nonlocal interaction may alter the characteristic Kondo energy scale,  $k_B T_K$ , and may lead to new regimes including ferromagnetically locked spins or an interimpurity singlet [38–40]. Indeed, our model system covers the range from weakly coupled Kondo atoms to interimpurity exchange coupling that is comparable to the Kondo energy scale.

Figure 2.5 presents the main experimental findings [34]. It shows the  $dI/dV$  signature of the Kondo resonance of one of the Co atoms in  $\text{CoCu}_n\text{Co}$  ( $1 \leq n \leq 6$ ) chains on Cu(111) together with STM images of the assemblies.  $dI/dV$  data were fit using (2.1) (black line in Fig. 2.5). The extracted Kondo temperatures exhibit a remarkable variation with the number of Cu atoms connecting the Co atoms.  $T_K$  nearly doubles from  $n = 1$  ( $T_K \approx 46$  K) to  $n = 2$  ( $\approx 79$  K), increases further to  $\approx 108$  K for  $\text{CoCu}_3\text{Co}$ , and then oscillates ( $\approx 93$ , 110, and 91 K for  $n = 4$ –6, respectively). For clarity these results are summarized in Fig. 2.6. The maxima of the oscillation match the Kondo temperature of a Co atom at the end of  $\text{Cu}_3$  and  $\text{Cu}_4$  chains ( $\tilde{T}_K = 110$  K), which approximate a  $\text{CoCu}_\infty$  chain (dashed line in Fig. 2.6).

The calculations of [34] first showed that single-impurity Kondo physics cannot reproduce the experimentally observed variation of  $T_K$ . In the absence of magnetic



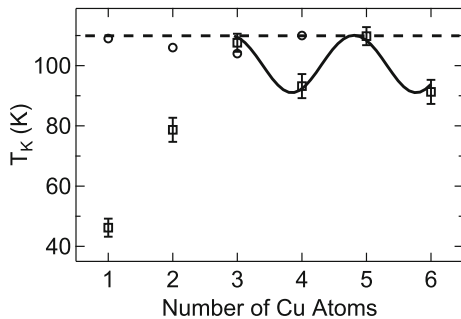


**Fig. 2.6**  $T_K$  of  $\text{CoCu}_n\text{Co}$  chains versus  $n$  (squares). The Kondo temperature  $\tilde{T}_K = 110$  K of a single Co adatom at the end of a  $\text{Cu}_4$  chain is indicated by a dashed line. Calculated *single-impurity* Kondo temperature, that would be expected in the absence of magnetic Co–Co interactions, are indicated as circles. The calculated periodicity in the RKKY interaction regime is shown as a sinusoidal line. Reprinted with permission from N. Néel et al., Phys. Rev. Lett. **107**, 106804 (2011) [34]. Copyright 2011 by the American Physical Society

Co–Co interactions in  $\text{CoCu}_n\text{Co}$  chains the calculated variation of  $T_K$  (circles in Fig. 2.6) is much smaller than in the experiments and does not even follow the trend of the experimental data.

In a second step magnetic coupling between the Co atoms was introduced. For the relaxed  $\text{CoCuCo}$  chain an exchange interaction energy  $E_{\text{ex}} = E_{\uparrow\downarrow} - E_{\uparrow\uparrow} = 14 \pm 6$  meV was found giving rise to ferromagnetic ( $\uparrow\uparrow$ ) coupling of the Co atoms. An antiferromagnetic ( $\uparrow\downarrow$ ) interaction with  $E_{\text{ex}} = -17 \pm 3$  meV couples the Co atoms in  $\text{CoCu}_2\text{Co}$  linear chains. Despite the ferromagnetic Co–Co interaction in  $\text{CoCuCo}$  chains, a Kondo resonance with  $T_K = 46$  K is observed. The interplay of the coupling between the impurities,  $H = -JS_1 \cdot S_2$ , and Kondo screening was addressed theoretically in terms of two-site spin-1/2 Kondo models [38–40]. If the exchange interaction is ferromagnetic ( $J > 0$ ) and dominates over the Kondo energy scale of the single-impurity ( $k_B\tilde{T}_K \ll J$ ), the two spins lock to a total spin,  $S_1 + S_2 = 1$ , and give rise to a spin-1 Kondo effect [38]. This results in a reduced Kondo temperature,  $T_K \approx k_B\tilde{T}_K^2/J$ , which with  $T_K = 46$  K,  $\tilde{T}_K = 110$  K,  $E_{\text{ex}} = 14 \pm 6$  meV is compatible with the experiments. Consequently, Co atoms in the  $\text{CoCuCo}$  linear chains are in a crossover regime between two independent and two ferromagnetically locked Kondo atoms, for which a narrower rather than a completely suppressed Kondo resonance is found.

For  $\text{CoCu}_2\text{Co}$  the calculations revealed  $|E_{\text{ex}}| \approx 2 k_B\tilde{T}_K$  [34], which is close to the quantum critical point at  $J \approx 2.2 k_B\tilde{T}_K$  predicted for two-site spin-1/2 Kondo impurities in the particle-hole-symmetric case. At this critical point a ground state with an antiferromagnetically locked interimpurity singlet is separated from a ground state of two individually screened Kondo impurities [39, 40]. If particle-hole symmetry is lost, a crossover region replaces the quantum critical point, and the Kondo resonance continuously evolves into a pseudogap feature [41–46]. This crossover region has two characteristic energy scales  $T_L < T_H$  which represent spin fluctuations and

quasiparticle excitations [41–44, 46]. The lower energy scale,  $T_L$ , gives rise to the sharper and more pronounced feature in the spectral function at  $E_F$  [44] and characterizes the onset of local Fermi liquid behavior [46]. Hence,  $k_B T_L$  should correspond to the experimentally observed width of the Kondo resonance with  $T_L = T_K$ . As  $T_L < T_K$  [41–44, 46], a narrowed Kondo resonance is consistent with the crossover regime and in agreement with the experimental observation. As an important result we obtained that ferromagnetic and antiferromagnetic interactions lead to  $T_K < \tilde{T}_K$  [47, 48].

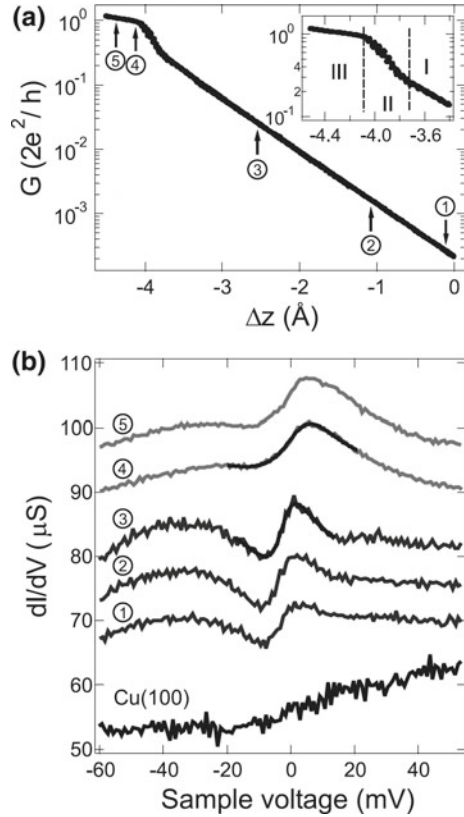
The oscillations of  $T_K$  for  $n \geq 3$  result from the RKKY interaction between the Co atoms. To show this, the Fermi wave vector,  $k_F$ , was determined for  $\text{Cu}_\infty$  chains on Cu(111) as  $k_F \approx 0.37 \cdot (2\pi/a)$  with  $a = 2.57 \text{ \AA}$  the Cu(111) lattice constant. Therefore, Co–Co RKKY interactions oscillate with  $2k_F \approx 0.74 \cdot (2\pi/a)$ , which by subtracting a reciprocal lattice vector is identical with  $-0.26 \cdot (2\pi/a)$  and corresponds to a direct-space periodicity of  $\approx 3.8a$ . While this spatial periodicity can be seen in the oscillatory magnetization density along  $\text{CoCu}_n\text{Co}$  ( $n \geq 3$ ) chains [34], it differs from the periodicity observed for  $T_K$ . For weak RKKY interactions,  $\tilde{T}_K^2 - T_K^2 \approx E_{\text{ex}}^2/k_B^2$  [34, 47, 48], with  $E_{\text{ex}}^2 \propto [\sin(2k_F n a)]^2$ . Therefore, the spatial periodicity is reduced to  $\approx 1.9a$ , which corresponds to the even-odd oscillations of  $T_K$  in the experiments. In conclusion, the two-site Kondo effect has been addressed by  $\text{CoCu}_n\text{Co}$  atomic chains. Co–Co magnetic interactions ranging from ferromagnetic coupling ( $n = 1$ ) via an antiferromagnetic singlet ( $n = 2$ ) to RKKY interaction ( $n \geq 3$ ) have been probed using line shape variations of the Kondo resonance.

### 2.1.4 Spectroscopy of the Kondo Resonance at Contact

Deviating from the preceding paragraphs where the Kondo resonance was probed by  $dI/dV$  spectroscopy in the tunneling range, spectroscopies are now performed close to and at contact between the STM tip and the magnetic impurity. In particular, single-atom junctions will be considered where currents on the order of  $1 \mu\text{A}$  flow across the Kondo atom, which corresponds to a junction conductance on the order of the quantum of conductance,  $G_0 = 2e^2/h$  ( $e$ : elementary charge,  $h$ : Planck constant). The break junction technique, in which thin metal wires are ruptured, was used to measure the conductances of metallic nanowires [49]. STM experiments enable imaging of the contact region prior to and after contacting the atom of interest. Modifications of the junction, such as atom transfer [50–52], that could change the electronic properties may be identified and avoided. Moreover, the electrodes and the contacted atom may be chosen independently as different materials, which is particularly appealing for Kondo atoms on nonmagnetic substrate surfaces.

Figure 2.7a shows a typical conductance trace acquired simultaneously with a tip approach towards a single Co atom on Cu(100) [inset to Fig. 2.7a] [27]. As detailed in [53, 54] the exponential part of the conductance curve reflects the tunneling range (region I), which is followed by region II reflecting the transition to the contact range (III). The latter is reached at a junction conductance of  $\approx 1 G_0$ .

**Fig. 2.7** **a** Conductance  $G$  as a function of tip displacement  $\Delta z$ . Inset: Transition (II) from the tunneling (I) to the contact (III) range. **b**  $dI/dV$  spectra taken at tip displacements shown in (a). Bottom curve: Spectrum of the bare Cu(100) surface at  $5 \mu\text{A}$ . Curves 1, 2 and 3 show  $dI/dV$  spectra of a single Co atom in the tunneling range at 1 nA, 10 nA, 100 nA. Spectra 4 and 5 were taken in the contact range at currents of  $5.5 \mu\text{A}$  and  $6 \mu\text{A}$ , respectively. Calculated Fano profiles using the parameters  $q = 1.2$ ,  $T_K = 78 \text{ K}$  (spectrum 3) and  $q = 2.1$ ,  $T_K = 137 \text{ K}$  (spectrum 4) are shown as solid lines. Reprinted with permission from N. Néel et al., Phys. Rev. Lett. **98**, 016801 (2007) [27]. Copyright 2007 by the American Physical Society



In Fig. 2.7b  $dI/dV$  spectra in the tunneling (1, 2, 3) and the contact range (4, 5) are presented together with a tunneling  $dI/dV$  spectrum on clean Cu(100) for comparison. The Kondo resonance appears with an asymmetric line shape around zero bias voltage, in agreement with a previous report [55]. Intriguingly, this resonance is likewise observed in the contact range, albeit broadened.

Figure 2.8 summarizes the experimentally obtained Kondo temperatures (triangles) as extracted from fits of (2.1) to  $dI/dV$  data together with calculated data (circles). Both data sets exhibit an abrupt change of  $T_K$  at  $\Delta z \approx -4.1 \text{ \AA}$ . For  $\Delta z > -4.1 \text{ \AA}$  experimental and calculated  $T_K$  vary between 70 and 100 K. In the contact range,  $\Delta z < -4.1 \text{ \AA}$ , experimental values for  $T_K$  vary between 140 K and 160 K while calculated data scatter within 200–290 K. The sudden broadening of the Kondo resonance upon contact can thus be related to an abrupt increase of  $T_K$ .

For the calculation of the Kondo temperature the single-impurity Anderson model [6, 25, 56] was used. In this model  $T_K$  reads

$$T_K = \frac{1}{k_B} \sqrt{\frac{\Delta U}{\pi}} \exp \left[ -\frac{\pi}{\Delta} \left( \left| \frac{1}{\varepsilon_d} \right| + \left| \frac{1}{\varepsilon_d + U} \right| \right)^{-1} \right] \quad (2.7)$$

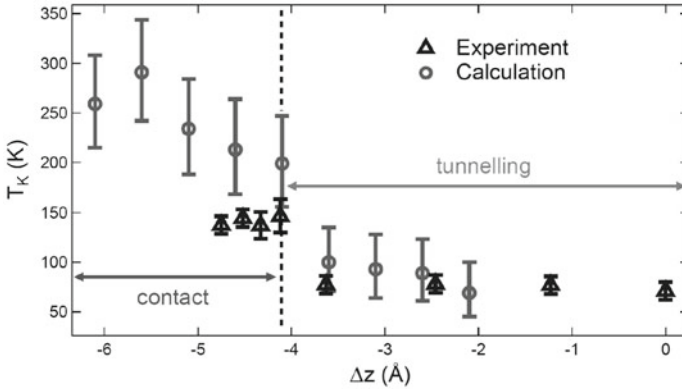


**Fig. 2.8** Kondo temperature  $T_K$  versus tip displacement  $\Delta z$ . Experimental data are depicted by triangles, theoretical data are presented by circles. The dashed line separates tunnelling and contact ranges. Reprinted with permission from N. Néel et al., Phys. Rev. Lett. **98**, 016801 (2007) [27]. Copyright 2007 by the American Physical Society

( $\Delta$ : width of the impurity state,  $\varepsilon_d$ : energy of occupied  $d$  band center with respect to  $E_F$ ,  $U$ : on-site Coulomb interaction energy between spin-up and spin-down states). In the case of several impurity levels, as for the Co  $d$  states,  $\Delta$  reflects the broadening due to the crystal field splitting between these states. Using density functional theory  $\Delta$ ,  $\varepsilon_d$ ,  $U$  are accessible from ground state calculations. We found that the main changes during tip approach occur in the spin-up states of the Co atom [27]. The closer proximity of the tip induces a shift of these states towards  $E_F$ —thus reducing the exchange splitting—and a broadening of the individual peaks. This behavior reflects the additional hybridization of the adsorbed Co atom with the tip. Indeed, the crystal field splitting increases from  $\Delta = 0.24$  eV in the tunnelling range to  $\Delta = 0.40$  eV in the contact range.

While the increase of  $T_K$  upon contact is well reproduced by the calculations, the actual values for  $T_K$  deviate from experimental data. These deviations may in part be due to the rather simple model that does not do justice to the complex junction. In addition, the surface-atom-tip system considered in the simulations is very rigid due to the limited number of layers on either side of the contacted atom. An increased  $T_K$  has likewise been observed in more recent experiments on Co-covered Cu(100) [57].

The above experiments were extended by using a Cu(111) substrate and different tip materials, nonmagnetic Cu-coated W and ferromagnetic bulk Fe tips [58]. The observed broadening of the Kondo resonance is not due to a voltage drop at the transimpedance amplifier, nor do local heating effects play a significant role [52]. However, to some extent, the broadening may be due to a change of the adatom's electrostatic potential. While it is pinned to the sample potential in the tunnelling range, this may change at contact [59]. In contrast to results obtained for Co on Cu(100) [27] the width of the Kondo resonance does not increase upon contact with Cu-coated

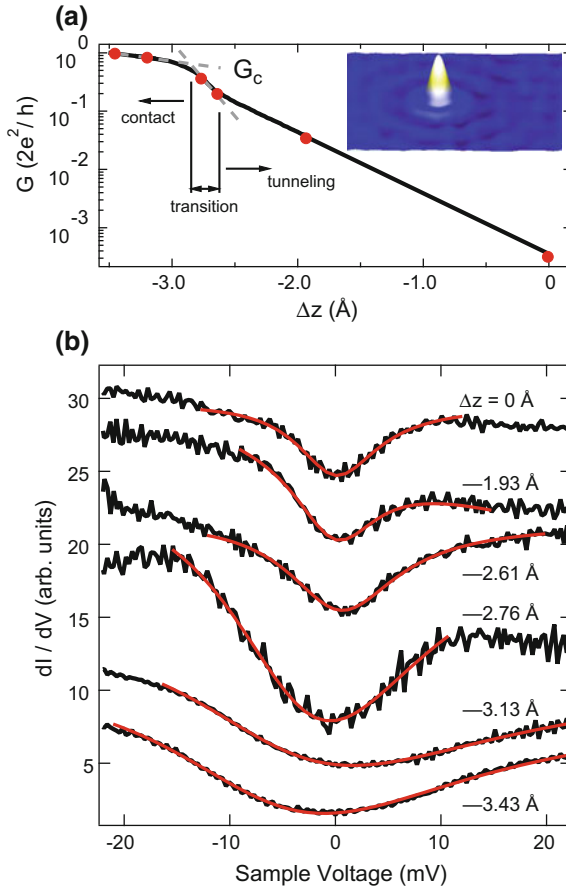
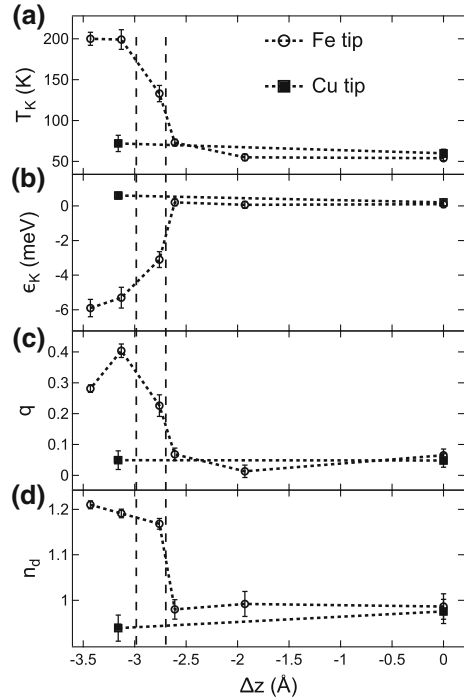


**Fig. 2.9** **a** Conductance curves of a Co atom on Cu(111) versus displacement of a Fe tip. Tunneling, transition and contact ranges are indicated. The conductance trace between 0 and  $\approx -2$  Å is an exponential extrapolation of tunneling conductance in the displacement range from  $\approx -2$  to  $-2.5$  Å. The contact conductance,  $G_c$ , is defined by the intersection of linear fits (dashed lines) to conductance data in the contact and transition ranges. Zero displacement is defined by the parameters of the feedback loop (33 mV and 1 nA). Inset: STM topograph of a single Co atom on Cu(111) ( $8$  Å  $\times$   $8$  Å, 33 mV, 1 nA). **b**  $dI/dV$  spectra acquired at conductances, that are indicated on the conductance trace by dots (**a**). Fits of Fano resonance to the experimental spectra are shown as solid lines. Reprinted with permission from N. Néel et al., Phys. Rev. B 82, 233401 (2010) [58]. Copyright 2010 by the American Physical Society

W tips, which is in agreement with a previous report [60]. However, hybridization with Fe tips leads to a significant broadening. Figure 2.9a shows the evolution of the single-Co junction conductance depending on the Fe tip displacement. While the transition between tunneling and contact ranges is gradual as observed in contact experiments for Co on Cu(100) with a Cu-coated W tip, the contact conductance is slightly lower,  $G_c \approx 0.7 G_0$ . In Fig. 2.9b the evolution of the  $dI/dV$  signature of

**Fig. 2.10** **a** Kondo temperature  $T_K$ , **b** resonance energy  $\varepsilon_K$  **c** asymmetry factor  $q$  for a Co atom on Cu(111) contacted with a Cu-coated W (upright triangles) and Fe (rotated triangles) tip versus tip displacement  $\Delta z$ . Uncertainty margins result from fitting multiple  $dI/dV$  spectra. Vertical dashed lines separate tunneling, transition and contact ranges as introduced in Fig. 2.9a. **d** The occupation number  $n_d$  of the Co  $d$  orbitals versus  $\Delta z$ .  $n_d$  was calculated using (2.8) with fitted  $T_K$  (a)  $\varepsilon_K$  (b). Reprinted with permission from N. Néel et al., Phys. Rev. B 82, 233401 (2010) [58]. Copyright 2010 by the American Physical Society



the single-Co Kondo resonance obtained with a Fe tip from tunneling to contact is presented.

Fits to  $dI/dV$  data according to (2.1) appear as solid lines and lead to  $T_K$ ,  $q$ ,  $\varepsilon_K$  as a function of the tip displacement  $\Delta z$  (Fig. 2.10). In the tunneling range ( $\Delta z > -2.65$  Å) these parameters are almost equal and constant for both tip materials, which reflects that the interaction between the tip and the sample is negligible in this conductance range. Starting from the transition range, however, Fe and Cu-coated W tips lead to strikingly different results. For Fe tips all parameters start to deviate from their tunneling range values.  $T_K$  [Fig. 2.10a] increases from  $\approx 60$  to  $\approx 130$  K, the  $\varepsilon_K$  [Fig. 2.10b] drops from  $\approx 0$  to  $-3$  meV, and  $q$  [Fig. 2.10c] increases from  $\approx 0.05$  to  $0.25$ . At contact this trend is continued with  $T_K \approx 200$  K,  $\varepsilon_K \approx -6$  meV,  $q \approx 0.3$ – $0.4$ . For Cu-coated W tips all parameters are essentially constant throughout tunneling, transition and contact ranges.

The hybridization seems to be determined by chemical identity of the atom at the tip apex. A splitting of the Kondo resonance due to a magnetic stray field from the Fe tip at the adatom site would be too low to explain the observed broadening. The dipole field can be estimated to be  $H \approx 1$  T at contact [61], which would result in a splitting of  $\approx 2g\mu_B H \approx 0.2$  meV ( $g$ : Landé factor,  $\mu_B$ : Bohr magneton) [62]. This is more than one order of magnitude lower than  $k_B T_K$  with  $T_K \approx 60$  K.

The line shape parameter  $q$  increases significantly upon contact formation between the Co adatom and the Fe tip, which reflects the additional hybridization of Co  $d$  levels with Fe states. The  $d$  bands of ferromagnetic Fe are located around at  $E_F$  [63, 64] and may hybridize with the Co  $d$  states. In contrast, the copper  $d$  bands are well below  $E_F$  [65], which hampers effective hybridization and results in an almost constant  $q$ . In the tunneling range,  $d$  states decay much faster into the vacuum compared to  $s$  states [66], so that  $s$  states dominate the hybridization, which results in similar  $q$  values for Cu-coated W and Fe tips. The different hybridization results in a change of the Co  $d$  state occupation number,  $n_d$ , which is related to  $\varepsilon_K$  and  $T_K$  via [6, 25]:

$$n_d = 1 - \frac{2}{\pi} \tan^{-1} \left( \frac{\varepsilon_K}{k_B T_K} \right) \quad (2.8)$$

and may be extracted from the fit parameters. For this, we assume that only a single Co  $d$  level hybridizes with the tip. This assumption can be justified by a theoretical study of a Co adatom on Au(111) [25] which showed that due to  $sp-d$  hybridization four Co  $d$  orbitals are completely filled while one partially occupied orbital ( $n_d = 0.8$ ) is responsible for the Kondo effect. Empty, half-filled, and filled  $d$  levels correspond to  $n_d = 0, 1$ , and  $2$ , respectively. Figure 2.10d displays  $n_d$  obtained from (2.8) as a function of  $\Delta z$  for Fe and Cu-coated W tips. Clearly,  $n_d$  changes upon contact from  $\approx 0.98$  (average value in the tunneling range) to  $\approx 1.2$  (contact) while it remains almost constant for the Cu-coated W tip ( $\approx 0.98$ ). A value of  $n_d \approx 0.98$  is in good agreement with  $n_d$  obtained for Co atoms on Cu(111), while  $n_d \approx 1.2$  comes close to the value of a Co atom on Cu(100) [30]. Recent work using Ni tips [67] showed that a splitting of the Kondo resonance due to the exchange field is possible and may contribute to the broadened feature observed here for Fe tips. In summary, the hybridization with the tip apex atom changes in the crystal field splitting and the  $d$  level occupation, which affects  $T_K$ .

## 2.2 Magnetic Molecules

Magnetic sandwich complexes are of particular interest for investigating interactions between molecular spin centers. Localized magnetic moments also interact with the conduction electrons of non-magnetic substrates, which may lead to a Kondo resonance that serves as a convenient read-out channel.

### *Benzene-Bridged Cobaltocene-Like Complexes*

To explore the above approach, a trinuclear sandwich complex interconnected by benzene linkers (1,3,5-tris-( $\eta^6$ -borabenzene- $\eta^5$ -cyclopentadienyl)cobalt), TCBB, Fig. 2.11a) was synthesized following [68] and [69]. TCBB was deposited on Cu(111) using an electrospray ionization (ESI) setup with mass selection [70].

During the deposition process some fragmentation of TCBB occurs. However, besides  $\eta^6$ -borabenzene- $\eta^5$ -cyclopentadienylcobalt monomers and dimers intact TCBB molecules are frequently observed. Figure 2.11b displays a typical topograph,

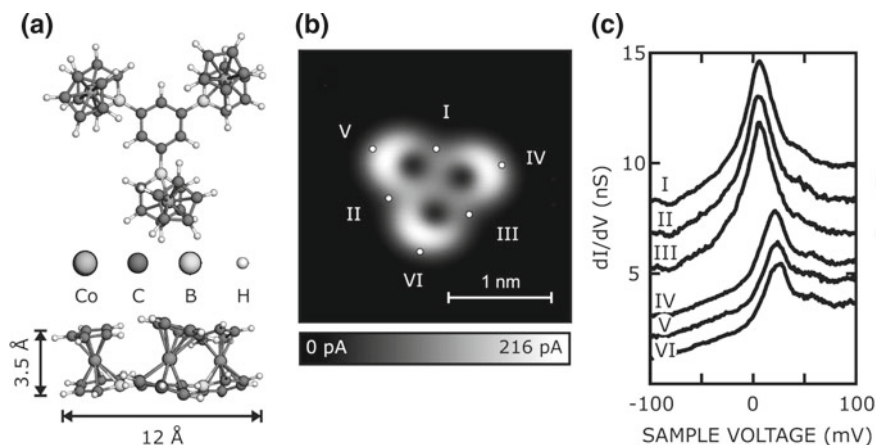


**Fig. 2.11** **a** Top and side views of the calculated gas-phase structure of TCBB. **b** Constant-height image ( $V = 0.1$  V) of TCBB on Cu(111). Markers indicate positions where  $dI/dV$  spectra were recorded. **c** Spectra, vertically shifted for clarity. STM images have been processed with WSxM [71]. Reprinted with permission from T. Knaak et al., *Nano Lett.* **17**, 7146 (2017) [72]. Copyright 2017 American Chemical Society

which clearly shows the clover-like shape of TCBB lying flat on the substrate. Owing to a tilt of the CBB units towards the center of the molecule, the depressions (dark spots) corresponding to the centers of the Cp rings are slightly displaced from the center of the surrounding protrusions [73, 74].

Spectra of the differential conductance acquired at several positions above a TCBB molecule (Fig. 2.11c) show a clear peak close to the Fermi level  $E_F$ , which we attribute to a Kondo resonance. Interestingly, the resonance energy and lineshape vary in a systematic fashion between these positions. In particular, the shift of the resonance peak from  $E_F$  is  $\varepsilon_K = 5.1$  meV at positions I–III, while  $\varepsilon_K = 22.2$  meV at positions IV–VI. However, this variation does not reflect the interaction of the Co centers, because identical spectroscopic features are found on CBB monomers and dimers as well. Mapping of the position of the Kondo resonance on monomers showed that the areas with  $\varepsilon_K = 5.1$  meV match the calculated spatial distributions of the singly occupied molecular orbital (SOMO, mainly  $d_{yz}$  character) whereas the areas with  $\varepsilon_K = 22.2$  meV match the lowest unoccupied molecular orbital (LUMO, mainly  $d_{xz}$ ). A Kondo resonance occurs for partially filled orbitals, a condition that is obviously met by the SOMO. The  $d_{xz}$ , which is empty in the gas-phase molecules, is broadened by the interaction with the substrate giving rise to a possible charge transfer. The occupation number  $n_d$  of a localized state involved in the Kondo resonance may be estimated from (2.8). Fits to the experimental spectra yield  $n_d \approx 0.9$  and  $0.5$ , which is consistent with the above interpretation. So far, experimental results on multiple Kondo resonances from a single molecule had been rather scarce [75, 76]. In contrast to magnetic adatoms, where the orbitals at the origin of Kondo resonances may be degenerate and spatially overlap, the ligand field in molecular systems can



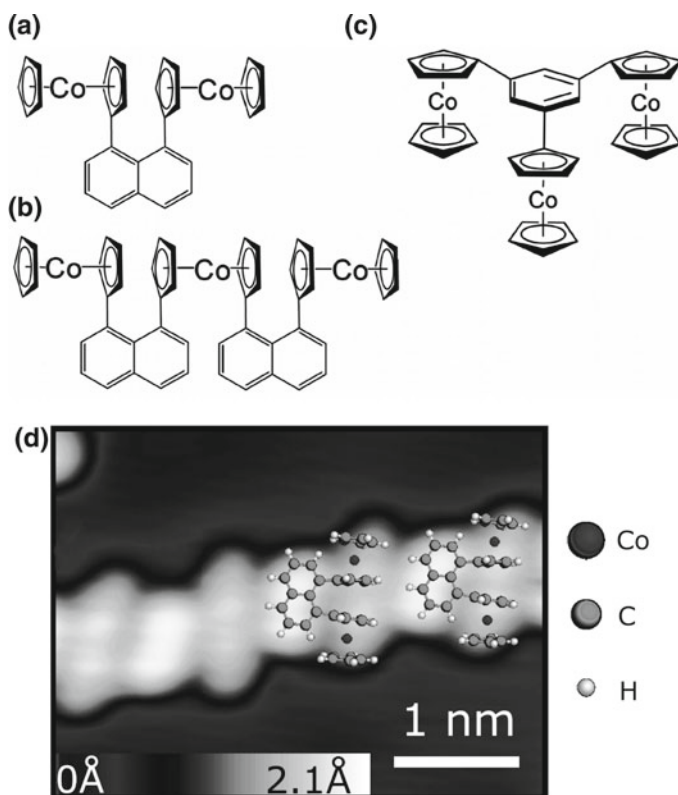


**Fig. 2.12** **a** Benzene-bridged triscobaltocene (BTC). **b** Naphthalene-bridged biscobaltocene (NBC). **c** Naphthalene-bridged triscobaltocene (NTC). **d** STM topograph of a NBC chain on Au(111).  $I = 30$  pA,  $V = 0.2$  V. Scaled models of NBC are superimposed. Reprinted with permission from T. Knaak et al., *J. Phys. Chem. C* **121**, 26777 (2017) [77]. Copyright 2017 American Chemical Society

strongly influence the degeneracy and the extent of the orbitals relevant for the Kondo resonances.

#### *Benzene- and Naphthalene Bridged Cobaltocenes*

Benzene-bridged triscobaltocene (Fig. 2.12a, BTC) seems rather similar to TCBB and other metallocenes [72, 73, 78]. The cobaltocene ( $\text{CoCp}_2$ ) subunits should carry a spin  $\frac{1}{2}$ . However, we did not observe any zero-bias feature reminiscent of a Kondo effect from BTC on Au(111). Topographs of BTC, however, suggest that the  $\text{CoCp}_2$  subunits are significantly tilted whereas the magnetic units of the TCBB molecules are nearly perpendicular on the substrate. We tentatively suggest that the large tilt reduces the coupling of the localized spins to the substrate, which effectively prevents a Kondo effect.

For further comparison, we investigated naphthalene-bridged bis- and triscobaltocene (Fig. 2.12b and c, NBC and NTC). It turned out that both compounds adsorb with the  $\text{CoCp}_2$  subunits oriented parallel to the surface. Figure 2.12d shows a topograph of NBC with the proposed adsorption geometry indicated by an overlaid model of the molecules. This geometry is motivated by the fact that a perpendicular orientation is sterically hindered. This leads to an angle between the naphthalene and the Cp-ring planes of  $\approx 47^\circ$  in the gas phase. On the substrate, a gain in interaction energy is expected as the angle is further reduced. Moreover, spatially resolved  $dI/dV$  spectroscopy reveals Kondo resonances at the positions of the Co atoms in the model. The resonance amplitudes of the two subunits are different, presumably because the Co positions imposed by the naphthalene linker are incommensurate with the Au(111) lattice. No Kondo effect was found from NTC. We speculate that the additional geometrical constraints imposed by the two naphthalene linkers lead to insufficient Co-Au(111) coupling.

## 2.3 Graphene on Ir(111)

The direct interaction between a magnetic molecule or atom with a metallic substrate often has a drastic effect on the molecular or atomic properties. As a result, various approaches of tuning the degree of interaction with a substrate have been proposed. They include self-decoupling molecules like cyclophanes [79] or spacer layers of the relevant molecules themselves [80] or inorganic insulators [81, 82]. Graphene is particularly appealing, both for its excellent growth properties on various substrates and its unique electronic properties. As a substrate, Ir(111) is remarkable because an almost unchanged graphene band structure has been found [83]. The effect of the graphene layer on the electronic states of the Ir substrate has hardly been explored.

### *Graphene Islands*

To characterize the electronic structure of graphene on Ir(111) close to the Fermi level in nanoscale structures, we prepared nearly circular graphene islands with characteristic diameters of  $\approx 5 \dots 10$  nm [84]. Maps of the differential conductance  $dI/dV$  recorded above these islands (Fig. 2.13) reveal confined electronic states. In contrast to earlier reports, that interpreted similar data in terms of Dirac states of graphene, we attribute these states to confinement of the occupied electronic surface resonance of the Ir(111) substrate. As demonstrated by further STS data and DFT calculations, the interaction with the graphene layer shifts this state closer to the Fermi level. In other words, the islands effectively gate the Ir surface resonance. Confinement of the graphene states may also occur, but compared to the Ir resonance, which is located around the  $\bar{\Gamma}$  point of the surface Brillouin zone, their contribution to the tunneling current is minor, because they are centered around  $\bar{K}$  points. Their high in-plane momentum drastically reduces the tunneling probability.

### *W-H Complexes on Graphene*

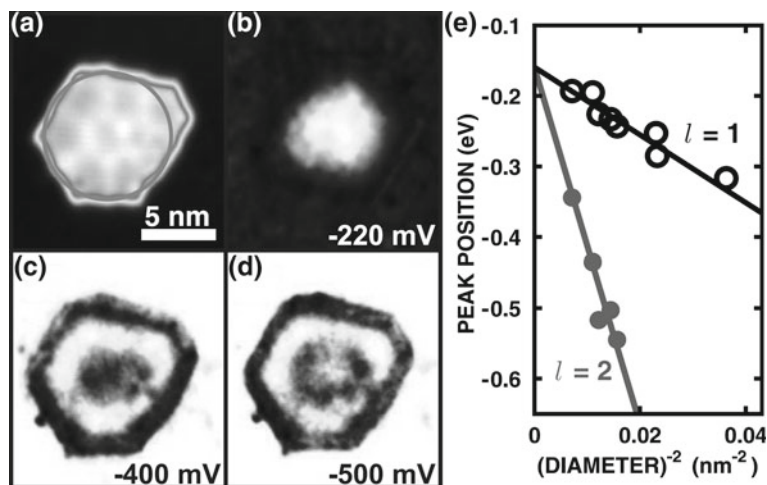


**Fig. 2.13** **a** Graphene island on Ir(111) imaged at  $-220$  mV and 1 nA. The effective island diameter of 8.3 nm used in modelling its electronic states is indicated by a light gray circle. **b–d** Normalized  $dI/dV$  maps of this island reveal LDOS oscillations as expected for the confinement of an electron gas in a quantum dot. **e** Data from various graphene islands show the energies of confined states with a principal quantum number ( $n = 0$ ). States with  $l = 1$  (circles) and  $l = 2$  (dots) are resolved. Lines show a fit involving the binding energy (160 meV) and the effective mass ( $0.18 m_e$ ) of an occupied Ir surface resonance. Reprinted with permission from S. Altenburg et al., Phys. Rev. Lett. **108**, 206805 (2012) [84]. Copyright 2012 by the American Physical Society

Single transition metal atoms on graphene may exhibit unusual properties such as large magnetic moments, which are often quenched on metallic substrates [85, 86], and may also exhibit an orbital Kondo effect [87]. We therefore prepared W adatoms on graphene on Ir(111) by sublimation [88]. It turned out that most of the W atoms reacted with hydrogen from the residual gas of the ultra-high vacuum system. These complexes may be dehydrogenated using the electric field of the STM tip and exhibit a number of peculiar effects, such as electric field induced shifts of spectroscopic features as well as reversible switching and charging effects. These observations for W are related to earlier reports of hydrogen-induced spectroscopic features of transition metal–hydrogen complexes [89, 90].

## 2.4 Ballistic Anisotropic Magnetoresistance of Single Atom Contacts

A fundamental consequence of spin-orbit coupling (SOC) is anisotropic magnetoresistance (AMR), i.e. the dependence of the electrical resistance on the direction of magnetization, which was predicted to be enhanced in ballistic electron transport through atomic scale junctions [91–95]. Although some experimental results [96,

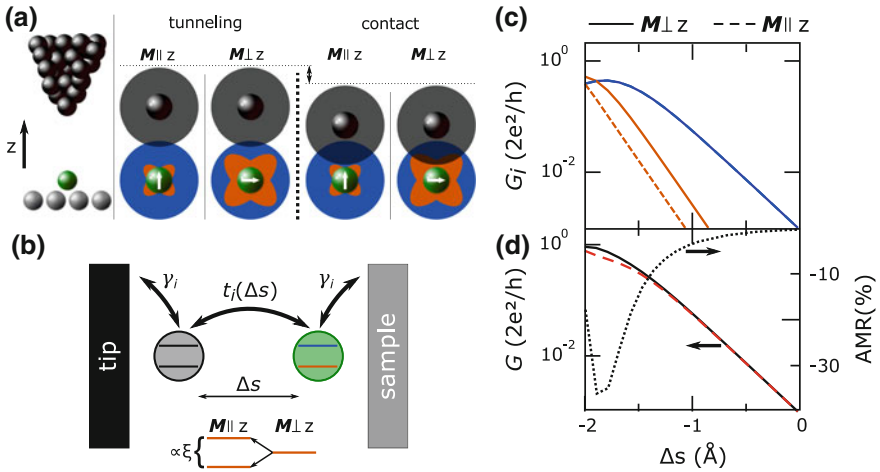


**Fig. 2.14** **a** Left: The STM tip (black) is positioned close to a single atom (green) on a substrate (gray). Right: The overlap between the orbitals of tip (black) and adatom (blue and orange) determines the current. The extent of the orange orbital (indicated as an isosurface of spectral electron density) changes with magnetization direction  $\mathbf{M}$  due to SOC. This orbital does not significantly contribute to the current at large tip-sample separations but becomes relevant in the contact regime. **b** simplified tight-binding scheme. Two localized states representing tip apex atom and adatom are coupled to metallic contacts using self-energy terms  $-i\gamma_i$  and mutually via hopping matrix elements  $t_i(\Delta s)$  that depend on the tip displacement  $\Delta s$  (defined relative to the distance in the tunneling regime).  $s$  (blue) and  $d_{xz,yz}$  (orange) states have a different spatial decay of the wavefunctions into the vacuum which affects  $t_i(\Delta s)$ . The change of the magnetization direction  $\mathbf{M}$  affects the splitting of  $d_{xz,yz}$  orbitals via SOC. **c** Conductance of different transport channels calculated versus separation  $\Delta s$ . **d** total conductance and resulting AMR. Reprinted with permission from J. Schöneberg et al., Nano Lett. **16**, 1450 (2016) [102]. Copyright 2016 American Chemical Society

97] were interpreted as ballistic AMR (BAMR), unambiguous experimental evidence of this effect is difficult to achieve. Large variations of its magnitude, likely due to the unknown atomic geometry of the junction [96, 98], suggested alternative interpretations such as telegraph noise [99], quantum fluctuations [100] and magnetostriction [101]. Here, we study BAMR without the need of an external magnetic field and thus eliminate magnetostriction, which could lead to artifacts by changing the junction geometry. We deposited single Co and Ir adatoms on the ferromagnetic Fe double layer on W(110), which provides different orientations of the magnetization direction due to its domain structure. By exchange interaction with the substrate, the magnetic moments of the adatoms can be oriented out-of-plane and in-plane when positioned on domains and domain walls, respectively. Nonmagnetic STM tips were brought into contact with these adatoms to determine the junction conductances on domains ( $G_d$ ) and domain walls ( $G_w$ ). These quantities were measured versus tip-sample displacement from the tunneling to the contact regime, yielding the AMR defined as  $\text{AMR} = (G_d - G_w)/G_d$ .

A distance-dependent AMR is essentially caused by multiple transport channels that contribute differently in the tunnelling and in the contact regimes and that are differently affected by SOC. This may be demonstrated with a simplified microscopic model (Fig. 2.14) comprising a local SOC of the adatom's  $d$ -states and a different distance dependence of the tunnelling matrix element across the junction for different orbitals. Figure 2.14a sketches a model of the experimental situation and the orbitals that contribute to the current depending on their spatial overlap for two different tip sample separations and two different magnetization directions  $\mathbf{M}$ . For larger distances, a relevant overlap exists only between the tip and the adatom orbital that extends the furthest into the vacuum and as a consequence the AMR is only sensitive to SOC induced effects of the extended orbital and is not influenced by SOC related effects on a localized state. The latter, however, increasingly contributes to the current and also potentially to the AMR when the tip-sample distance is reduced.

The conductance as a function of tip-adatom separation can be modeled using a tight-binding description (Fig. 2.14b). Two atoms are coupled via hopping terms and attached to contacts via self-energy terms causing a broadening of the atomic states. The adatom is modeled with three orbitals  $s$ ,  $d_{xz}$  and  $d_{yz}$ , that each have a different decay length while both  $d$  states are assumed to be degenerate without SOC. The effect of SOC is included by a term  $H_{\text{SOC}} = \xi \mathbf{l} \cdot \mathbf{s}$  ( $\mathbf{l}$ : orbital momentum operator,  $\mathbf{s}$ : spin momentum operator,  $\xi$ : the SOC strength) in the Hamiltonian (details see [102]). The current is dominated by the weakly decaying  $s$  orbital in the tunnelling regime, while for smaller separations ( $\Delta s < -1.5 \text{ \AA}$ ), the  $d_{xz,yz}$  orbitals increasingly contribute (Fig. 2.14c). Their transmissions change under rotation of the magnetization, which can also be observed in the total conductance at small separations (Fig. 2.14d). The resulting AMR is negligible for large separations and becomes negative at contact.

To experimentally check this expectation, we prepared W(110) surfaces by repeated heating cycles in  $\text{O}_2$  atmosphere and intermediate short annealing up to a temperature of 2200 K. Fe double layers were grown by Fe evaporation from an electron beam evaporator or a filament at elevated substrate temperatures 500 K. Single Co and Ir atoms were adsorbed on the Fe double layer at sample temperatures of 10 K.

The Fe bilayer on W(110) has ferromagnetic domains with a magnetization direction pointing out-of-plane and an in-plane magnetization within the domain walls. Due to SOC the magnetization direction affects the LDOS and leads to contrast in  $dI/dV$  maps with non-magnetic tips [103] (Fig. 2.15a). Thus, the position of single atoms on the domain structure may be determined. According to DFT calculations, the magnetic moments of Co and Ir adatoms align parallel to the Fe magnetization due to exchange interaction [104, 105].

The conductance  $G$  was measured versus vertical tip displacement  $\Delta z$ . Here  $\Delta z = 0 \text{ pm}$  is defined by the tip-sample separation at which the feedback loop was opened. As the feedback parameters (Co:  $V = 50 \text{ mV}$ ,  $I = 1.1 \text{ \mu A}$ ; Ir:  $V = 100 \text{ mV}$ ,  $I = 0.5 \text{ \mu A}$ ) were identical for adatoms on domains and domain walls, this results in  $\text{AMR} = 0\%$  for  $\Delta z = 0 \text{ pm}$ .

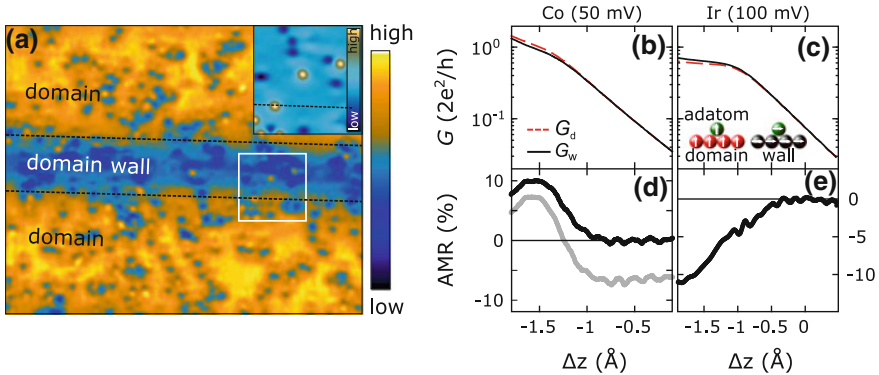


**Fig. 2.15** **a**  $dI/dV$  map ( $52 \times 42 \text{ nm}^2$ ,  $V = 70 \text{ mV}$ ,  $I = 0.5 \text{ nA}$ ) recorded on the double layer Fe on W(110) with single adsorbed Ir atoms. Domains and domain walls can be identified and marked by dashed lines. In the inset a constant current topograph ( $10 \times 10 \text{ nm}^2$ ,  $V = 100 \text{ mV}$ ,  $I = 50 \text{ pA}$ ) is shown, which was recorded in the area marked by a white square. From the comparison of  $dI/dV$  map and topograph, the atom in the middle can be identified to be positioned on a domain wall. **b** Conductance  $G$  versus tip displacement  $\Delta z$  recorded at  $V = 50 \text{ mV}$  (Co) and  $V = 100 \text{ mV}$  (Ir), respectively. Dashed (solid) curves correspond to data recorded on a domain ( $G_d$ ) (domain wall ( $G_w$ )). **d** and **e** show the AMR of Co and Ir adatoms. Reprinted with permission from J. Schöneberg et al., *Nano Lett.* **16**, 1450 (2016) [102]. Copyright 2016 American Chemical Society

The conductance versus displacement curves of both atoms show smooth transitions from the tunnelling regime to contact (Fig. 2.15b, c). At contact ( $\Delta z < -1 \text{ \AA}$ ) Co adatoms display a larger conductance on domains than on domain walls, in contrast to Ir atoms, for which  $G_d$  is smaller than  $G_w$  in the contact regime. This directly influences the AMR, which becomes negative for Ir and positive for Co at contact (black curves in Fig. 2.15d, e).

The above results demonstrate a BAMR of single-atom junctions containing either Co or Ir. The magnetoresistance at contact is  $\approx 10\%$  but different in sign for Co and Ir. This demonstrates that sign and magnitude of BAMR can be tuned by choosing suitable adatoms.

## 2.5 Shot Noise Spectroscopy on Single Magnetic Atoms on Au(111)

Compared with magnetoresistance, a less common approach to probe the influence of the electron spin on the electrical current through nanostructures is the analysis of current fluctuations [106–111]. Shot noise results from charge quantization and its power spectral density was derived by Schottky for vacuum diodes as  $S_0 = 2eI$ , [112]. In a quantum mechanical systems the Pauli principle causes anticorrelations between the electrons with identical spins [113] and decreases the shot noise. By

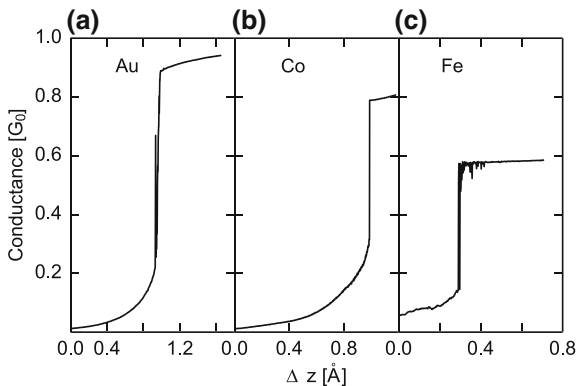


**Fig. 2.16** Conductance versus displacement of the tip towards the sample for contacts to single (a) Au, (b) Co, and (c) Fe atoms ( $V = 128$  mV). Reprinted with permission from A. Burtzloff et al., *Phys. Rev. Lett.* **114**, 016602 (2015) [115]. Copyright 2015 by the American Physical Society

this, spin-polarized electron transport may be identified and a lower boundary of the spin polarization can be extracted from the measurement. We implemented noise spectroscopy in a low temperature STM to probe spin effects in the transport through single atoms and molecules without requiring a magnetic tip, as used in SPSTM [114]. Single Au, Co and Fe atoms were evaporated onto a Au(111) surface and contacted with a Au covered W tip. While single Au atoms show a noise that is comparable to previous studies on mechanically controlled break junctions [109, 110], a significant reduction of current fluctuations below the minimum value for spin-degenerate transport can be observed on both, Fe and Co atoms.

Figure 2.16 shows current versus displacement curves,  $I(\Delta z)$ , of contacts to Au, Fe and Co atoms. The conductances at contact ( $V = 128$  mV) were 0.9–1.0  $G_0$  for Au (Fig. 2.1a),  $\approx 0.8 G_0$  for Co (Fig. 2.1b) while for Fe a considerably broader range of conductances between 0.47 and 0.68  $G_0$  (Fig. 2.16c) was observed.

To measure the noise, we used relays to switch the junction between the STM electronics and a low-noise battery driven power supply, that provides a constant bias current. Two home-built amplifiers measured the voltage fluctuations of the junction in parallel. These signals were cross-correlated to suppress the uncorrelated amplifier noise [116]. The low pass behavior ( $f_{-3\text{dB}} = 60$  kHz at  $G = 0.5 G_0$ ) caused by finite contact impedance and cabling capacitance was numerically compensated and the DC current was recorded by switching a current to voltage converter into the circuit before and after each noise measurement. We recorded STM images before and after each noise measurement, which occasionally showed atom movements, material transfer from tip to sample or a change of the imaging properties of the tip. In these cases the data were discarded and only data recorded on stable contacts were used for further analysis.

Figure 2.17 shows the spectral noise densities of Au (0.96  $G_0$ ) and Fe contacts (0.66  $G_0$ ) that were biased using identical currents. White noise is observed for

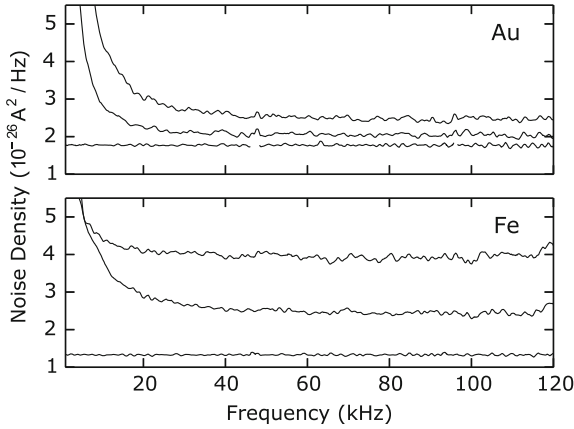


**Fig. 2.17** Current noise density of Au and Fe adatoms. The bias currents were 0 (lowest spectra), 0.17 and 0.34  $\mu\text{A}$ . The current noise increases significantly stronger with current for Fe compared with Au. The data has been smoothed using a moving average filter to simplify comparison. Reprinted with permission from A. Burtzloff et al., Phys. Rev. Lett. **114**, 016602 (2015) [115]. Copyright 2015 by the American Physical Society

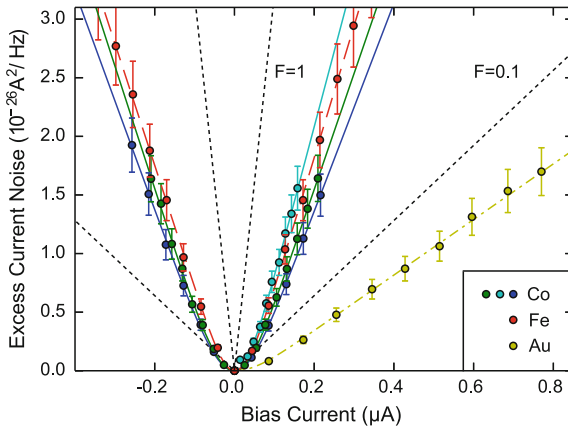


**Fig. 2.18** Excess noise power as a function of bias current. Fits of (2.10) to the experimental data (circles) from Fe, Au, and three Co atoms are shown in dashed, dash dotted, and solid lines. The Co data were measured using different tips and on different atoms. Slopes corresponding to Fano factors of  $F = 1$  and  $0.1$  are indicated as dotted lines. Reprinted with permission from A. Burtzloff et al., Phys. Rev. Lett. **114**, 016602 (2015) [115]. Copyright 2015 by the American Physical Society

$I = 0$ , which is caused by thermal current fluctuations. This Johnson-Nyquist noise  $S_{\ominus} = 4 k_B T G$  is larger for Au compared due to the higher conductance  $G$ . For  $I > 0$  additional noise contributions appear that increase significantly faster with bias current for Fe than for Au.



For further analysis the excess noise  $\Delta S$  was calculated by subtracting the  $I = 0$  spectrum, which contains  $S_\Theta$  and correlated amplifier noise (input current noise). The spectral density was averaged within a frequency interval (110–120 kHz) in which white noise was present and displayed as a function of bias current (Fig. 2.18).

In ballistic transport through nanostructures, the current is distributed over a finite number of conduction channels that are characterized by transmission probabilities  $\tau_i$  giving a total conductance  $G = G_0 \sum_i \tau_i$  [49]. Without spin degeneracy, each of these channels contains two spin channels  $j = (i, \sigma)$  ( $\sigma = \uparrow, \downarrow$ ) with potentially different transmission probability  $\tau_j$ . The degree of shot noise reduction due to electron correlations compared to the uncorrelated Poissonian noise  $S_0$  is quantified by the Fano factor, which is a function of  $\tau_j$ :

$$F = \frac{\sum_j \tau_j (1 - \tau_j)}{\sum_j \tau_j}. \quad (2.9)$$

Thus the Fano factor contains information on the transparencies  $\tau_j$  of the individual channels and their spin polarizations.

The excess noise as a function of bias current and at finite temperature can be written by the Lesovik expression [117]:

$$\Delta S = S - S_\Theta = F \left[ S_0 \coth \left( \frac{S_0}{S_\Theta} \right) - S_\Theta \right] \quad (2.10)$$

This equation was fitted to the experimental excess noise versus current curves of Fig. 2.18 with the temperature  $T$  and the Fano factor  $F$  as parameters.

Figure 2.19 shows Fano factors and conductances measured on different stable contacts to Fe, Co, and Au atoms. The lower boundary of the Fano factor in a spin-polarized (spin-degenerate) situation is indicated by a solid (dashed) line (cf. 2.9). The data for Au atoms reproduce prior results [109, 110]. Data from noise measurements on Co and Fe atoms lie between the solid and dashed lines indicating spin-polarized transmission. We observed this behavior in all valid measurements on Fe atoms and in all except one measurement on Co atoms.

Although one would expect that the high valency of Co and Fe atoms makes single-channel transport unlikely [118], DFT calculations (details see [115]) confirmed the presence of one dominating transport channel for both Fe and Co. This channel has  $\Gamma_1$  symmetry (invariant under rotations around the tip axis) as is the case for the  $s$ ,  $p_z$ , and  $d_{z^2}$  orbitals. The transmission probabilities of all other channels are lower by at least two orders of magnitude. This is due to the  $s$ -symmetry of the Au tip atom, which acts as an orbital filter, as the hybridization of other  $d$ - and  $p$ -orbitals of the adatom to the  $s$ -orbital of the tip is suppressed because of symmetry mismatch.

As the DFT calculations of our systems confirmed transport through one relevant channel (per spin), the spin polarization  $P = (\tau_\uparrow - \tau_\downarrow)/(\tau_\uparrow + \tau_\downarrow)$  can be extracted from the Fano factor. Dotted lines in Fig. 2.19 represent the Fano factors resulting from different degrees of spin polarization. The Fano factors measured on Co and Fe

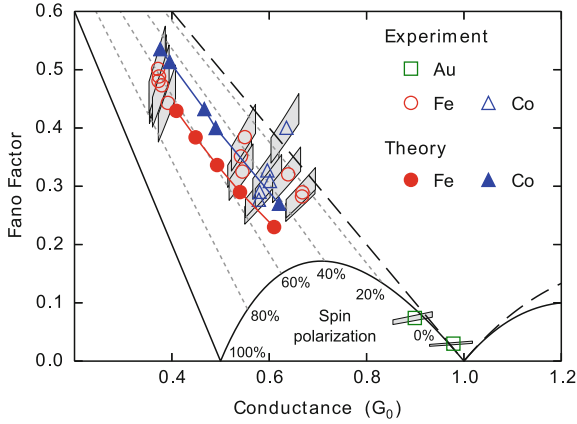


**Fig. 2.19** Fano factors  $F$  and conductances  $G$  of Au, Fe, and Co adatom contacts. The smallest possible Fano factors consistent with spin-polarized ( $P = 100\%$  up to  $0.5 G_0$ ) and spin degenerate ( $P = 0\%$  up to  $1 G_0$ ) transport are indicated as solid and dashed lines. For finite spin-polarizations, the Fano factors in a single channel scenario are plotted in gray dotted lines. Uncertainty margins are marked by gray areas. For Au the measured data are consistent with one single spin-unpolarized channel. For Co atoms 4 out of 5 data sets (recorded on different atoms with different tips) indicate a spin-polarized transmission involving a single channel. For Fe all data suggest single channel, spin-polarized transmission. Higher spin polarizations were observed on 5 data sets around  $0.38 G_0$ , that were all measured with the identical tip on different atoms in close vicinity to each other and to a step edge. Theoretical data was calculated for tip-adatom distances (left to right) of 4.10, 4.00, 3.95, 3.85, 3.70 Å (Fe) and 4.25, 4.20, 4.10, 4.05, 3.85 Å (Co). Reprinted with permission from A. Burtzclaff et al., Phys. Rev. Lett. **114**, 016602 (2015) [115]. Copyright 2015 by the American Physical Society

atoms around  $0.6\text{--}0.7 G_0$  correspond to spin-polarizations around 30–50%. Larger values of  $P$  ( $\approx 60\%$  for data around  $0.38 G_0$ ) were measured with a single tip on different Fe adatoms that were placed in close proximity to each other and to a nearby step edge. The role of the tip, a possible inter-atomic magnetic coupling and the electronic structure will be investigated in future experiments.

## References

1. W. Meissner, B. Voigt, *Annalen der Physik* **399**(8), 892 (1930)
2. J. Kondo, *Prog. Theor. Phys.* **32**(1), 37 (1964)
3. A.A. Abrikosov, *Physics* **2**, 5 (1965)
4. A.A. Abrikosov, *Physics* **2**, 61 (1965)
5. W. Marshall (ed.), *Theory of Magnetism in Transition Metals* (Academic, London, 1967), pp. 116–205
6. A.C. Hewson, *The Kondo Problem to Heavy Fermions* (Cambridge University Press, UK, 1993)
7. K. Yoshida, *Theory of Magnetism* (Springer, New York, 1996)
8. J.T. Li, W.D. Schneider, R. Berndt, B. Delley, *Phys. Rev. Lett.* **80**, 2893 (1998)

9. V. Madhavan, W. Chen, T. Jamneala, M.F. Crommie, N.S. Wingreen, *Science* **280**, 569 (1998)
10. M. Ternes, A.J. Heinrich, W.D. Schneider, *J. Phys.: Condens. Matter* **21**, 053001 (2009)
11. N. Nagaosa, J. Sinova, S. Onoda, A.H. MacDonald, N.P. Ong, *Rev. Mod. Phys.* **82**(2), 1539 (2010)
12. B.G. Park, J. Wunderlich, X. Martí, V. Holý, Y. Kurosaki, M. Yamada, H. Yamamoto, A. Nishide, J. Hayakawa, H. Takahashi et al., *Nat. Matter.* **10**(5), 347–351 (2011)
13. A. Manchon, H.C. Koo, J. Nitta, S.M. Frolov, R.A. Duine, *Nat. Matter.* **14**(9), 871 (2015)
14. J. Sinova, S.O. Valenzuela, J. Wunderlich, C.H. Back, T. Jungwirth, *Rev. Mod. Phys.* **87**(4), 1213 (2015)
15. C. Gould, C. Rüster, T. Jungwirth, E. Girgis, G.M. Schott, R. Giraud, K. Brunner, G. Schmidt, L.W. Molenkamp, *Phys. Rev. Lett.* **93**, 117203 (2004)
16. S.H. Yang, K.S. Ryu, S. Parkin, *Nat. Nanotechnol.* **10**(3), 221 (2015)
17. T. Uchihashi, J. Zhang, J. Kröger, R. Berndt, *Phys. Rev. B* **78**, 033402 (2008)
18. Z.Q. Qiu, N.V. Smith, *J. Phys.: Condens. Matter* **14**(8), R169 (2002)
19. J.E. Ortega, F.J. Himpsel, *Phys. Rev. Lett.* **69**, 844 (1992)
20. J.E. Ortega, F.J. Himpsel, G.J. Mankey, R.F. Willis, *Phys. Rev. B* **47**, 1540 (1993)
21. P. Bruno, *J. Phys.: Condens. Matter* **11**(48), 9403 (1999)
22. P. van Gelderen, S. Crampin, J.E. Inglesfield, *Phys. Rev. B* **53**, 9115 (1996)
23. R.K. Kawakami, E. Rotenberg, E.J. Escorcia-Aparicio, H.J. Choi, T.R. Cummins, J.G. Tobin, N.V. Smith, Z.Q. Qiu, *Phys. Rev. Lett.* **80**, 1754 (1998)
24. R.K. Kawakami, E. Rotenberg, E.J. Escorcia-Aparicio, H.J. Choi, J.H. Wolfe, N.V. Smith, Z.Q. Qiu, *Phys. Rev. Lett.* **82**, 4098 (1999)
25. O. Újsághy, J. Kroha, L. Szunyogh, A. Zawadowski, *Phys. Rev. Lett.* **85**, 2557 (2000)
26. M. Plihal, J.W. Gadzuk, *Phys. Rev. B* **63**, 085404 (2001)
27. N. Néel, J. Kröger, L. Limot, K. Palotas, W.A. Hofer, R. Berndt, *Phys. Rev. Lett.* **98**, 016801 (2007)
28. P. Wahl, P. Simon, L. Diekhöner, V.S. Stepanyuk, P. Bruno, M.A. Schneider, K. Kern, *Phys. Rev. Lett.* **98**, 056601 (2007)
29. P. Bruno, *Phys. Rev. B* **52**, 411 (1995)
30. P. Wahl, L. Diekhöner, M.A. Schneider, L. Vitali, G. Wittich, K. Kern, *Phys. Rev. Lett.* **93**, 176603 (2004)
31. O.O. Brovko, P.A. Ignatiev, V.S. Stepanyuk, P. Bruno, *Phys. Rev. Lett.* **101**, 036809 (2008)
32. N. Néel, J. Kröger, R. Berndt, T.O. Wehling, A.I. Lichtenstein, M.I. Katsnelson, *Phys. Rev. Lett.* **101**, 266803 (2008)
33. V. Madhavan, W. Chen, T. Jamneala, M.F. Crommie, N.S. Wingreen, *Phys. Rev. B* **64**, 165412 (2001)
34. N. Néel, R. Berndt, J. Kröger, T.O. Wehling, A.I. Lichtenstein, M.I. Katsnelson, *Phys. Rev. Lett.* **107**, 106804 (2011)
35. M.A. Ruderman, C. Kittel, *Phys. Rev.* **96**, 99 (1954)
36. T. Kasuya, *Prog. Theor. Phys.* **16**(1), 45 (1956)
37. K. Yosida, *Phys. Rev.* **106**, 893 (1957)
38. C. Jayaprakash, H.R. Krishna-murthy, J.W. Wilkins, *Phys. Rev. Lett.* **47**, 737 (1981)
39. B.A. Jones, C.M. Varma, *Phys. Rev. Lett.* **58**, 843 (1987)
40. B.A. Jones, C.M. Varma, J.W. Wilkins, *Phys. Rev. Lett.* **61**, 125 (1988)
41. O. Sakai, Y. Shimizu, T. Kasuya, *Solid State Commun.* **75**(2), 81 (1990)
42. O. Sakai, Y. Shimizu, *J. Phys. Soc. Jpn.* **61**(7), 2333 (1992)
43. O. Sakai, Y. Shimizu, *J. Phys. Soc. Jpn.* **61**(7), 2348 (1992)
44. O. Sakai, Y. Shimizu, N. Kaneko, *Physica* **186**, 323 (1993)
45. I. Affleck, A.W.W. Ludwig, B.A. Jones, *Phys. Rev. B* **52**, 9528 (1995)
46. L. Zhu, J.X. Zhu, *Phys. Rev. B* **83**, 195103 (2011)
47. V.Y. Irkhin, M.I. Katsnelson, *Z. Phys. B* **75**(1), 67 (1989)
48. V.Y. Irkhin, M.I. Katsnelson, *Phys. Rev. B* **56**, 8109 (1997)
49. N. Agraí, A.L. Yeyati, J.M. van Ruitenbeek, *Phys. Rep.* **377**(2), 81 (2003)

50. L. Limot, J. Kröger, R. Berndt, A. Garcia-Lekue, W.A. Hofer, *Phys. Rev. Lett.* **94**, 126102 (2005)
51. J. Kröger, H. Jensen, R. Berndt, *New J. Phys.* **9**(5), 153 (2007)
52. J. Kröger, N. Néel, A. Sperl, Y.F. Wang, R. Berndt, *New J. Phys.* **11**(12), 125006 (2009)
53. J. Kröger, N. Néel, L. Limot, *J. Phys.: Condens. Matter* **20**(22), 223001 (2008)
54. R. Berndt, J. Kröger, N. Néel, G. Schull, *Phys. Chem. Chem. Phys.* **12**, 1022 (2010)
55. N. Knorr, M.A. Schneider, L. Diekhöner, P. Wahl, K. Kern, *Phys. Rev. Lett.* **88**, 096804 (2002)
56. P.W. Anderson, *Phys. Rev.* **124**, 41 (1961)
57. D.J. Choi, M.V. Rastei, P. Simon, L. Limot, *Phys. Rev. Lett.* **108**, 266803 (2012)
58. N. Néel, J. Kröger, R. Berndt, *Phys. Rev. B* **82**, 233401 (2010)
59. S. Karan, D. Jacob, M. Karolak, C. Hamann, Y. Wang, A. Weismann, A. I. Lichtenstein, R. Berndt, *Phys. Rev. Lett.* **115**, 016802 (2015). <https://www.doi.org/10.1103/PhysRevLett.115.016802>
60. L. Vitali, R. Ohmann, S. Stepanow, P. Gambardella, K. Tao, R. Huang, V.S. Stepanyuk, P. Bruno, K. Kern, *Phys. Rev. Lett.* **101**, 216802 (2008)
61. A. Kubetzka, M. Bode, O. Pietzsch, R. Wiesendanger, *Phys. Rev. Lett.* **88**, 057201 (2002)
62. T.A. Costi, *Phys. Rev. Lett.* **85**, 1504 (2000)
63. A.M. Turner, A.W. Donoho, J.L. Erskine, *Phys. Rev. B* **29**, 2986 (1984)
64. T. Nautiyal, S. Auluck, *Phys. Rev. B* **34**, 2299 (1986)
65. W.F. Krolikowski, W.E. Spicer, *Phys. Rev.* **185**, 882 (1969)
66. M. Häfner, J.K. Viljas, D. Frustaglia, F. Pauly, M. Dreher, P. Nielaba, J.C. Cuevas, *Phys. Rev. B* **77**, 104409 (2008)
67. D.J. Choi, S. Guissart, M. Ormaza, N. Bachellier, O. Bengone, P. Simon, L. Limot, *Nano Lett.* **16**, 6298 (2016)
68. U. Hagenau, J. Heck, E. Hendrickx, A. Persoons, T. Schuld, H. Wong, *Inorg. Chem.* **35**, 7863 (1996)
69. C. Lindström, Synthese und Charakterisierung mehrkerniger benzolverbrückter Cobalt-Sandwich-Komplexe. Ph.D. thesis, Universität Hamburg, 2016
70. C. Hamann, R. Woltmann, I.P. Hong, N. Hauptmann, S. Karan, R. Berndt, *Rev. Sci. Instrum.* **82** (2011)
71. I. Horcas, R. Fernández, J.M. Gómez-Rodríguez, J. Colchero, J. Gómez-Herrero, A.M. Baro, *Rev. Sci. Instrum.* **78**, 013705 (2007)
72. T. Knaak, M. Gruber, C. Lindström, M.L. Bocquet, J. Heck, R. Berndt, *Nano Lett.* **17**, 7146 (2017)
73. M. Ormaza, P. Abufager, N. Bachellier, R. Robles, M. Verot, T. Le Bahers, M.L. Bocquet, N. Lorente, L. Limot, *J. Phys. Chem. Lett.* **6**(3), 395 (2015)
74. N. Bachellier, M. Ormaza, M. Faraggi, B. Verlhac, M. Vérot, T. Le Bahers, M.L. Bocquet, L. Limot, *Phys. Rev. B* **93**, 195403 (2016)
75. K.J. Franke, G. Schulze, J.I. Pascual, *Science* **332**, 940 (2011)
76. G.E. Pacchioni, M. Pivetta, L. Gragnaniello, F. Donati, G. Autès, O.V. Yazyev, S. Rusponi, H. Brune, *ACS Nano* **11**(3), 2675 (2017)
77. T. Knaak, M. Gruber, C. Lindström, J. Heck, R. Berndt, *J. Phys. Chem. C* **121**, 26777 (2017)
78. M. Ormaza, N. Bachellier, M.N. Faraggi, B. Verlhac, P. Abufager, P. Ohresser, L. Joly, M. Romeo, F. Scheurer, M.L. Bocquet, N. Lorente, L. Limot, *Nano Lett.* **17**, 1877 (2017)
79. F. Matino, G. Schull, F. Köhler, S. Gabutti, M. Mayor, R. Berndt, *PNAS* **108**, 961 (2011)
80. X. Ge, C. Manzano, R. Berndt, L. Anger, F. Köhler, R. Herges, *J. Am. Chem. Soc.* **131**, 6096 (2009)
81. S. Fölsch, A. Helms, S. Zöphel, J. Repp, G. Meyer, K.H. Rieder, *Phys. Rev. Lett.* **84**, 123 (2000)
82. S. Abbet, U. Heiz, H. Häkkinen, U. Landman, *Phys. Rev. Lett.* **86**, 5950 (2001)
83. I. Pletikosić, M. Kralj, P. Pervan, R. Brako, J. Coraux, A.T. N'Diaye, C. Busse, T. Michely, *Phys. Rev. Lett.* **102**, 056808 (2009)
84. S.J. Altenburg, J. Kröger, T.O. Wehling, B. Sachs, A.I. Lichtenstein, R. Berndt, *Phys. Rev. Lett.* **108**, 206805 (2012)

85. Y. Zhang, W. Ong, I. Arakelyan, J.E. Thomas, *Phys. Rev. Lett.* **108**, 235302 (2012)
86. S. Frota-Pessôa, *Phys. Rev. B* **69**, 104401 (2004)
87. T.O. Wehling, A.V. Balatsky, M.I. Katsnelson, A.I. Lichtenstein, A. Rosch, *Phys. Rev. B* **81**, 115427 (2010)
88. S.J. Altenburg, R. Berndt, *New J. Phys.* **16**, 093047 (2014)
89. M. Pivetta, M. Ternes, F. Patthey, W.D. Schneider, *Phys. Rev. Lett.* **99**, 126104 (2007)
90. F. Natterer, F. Patthey, H. Brune, *Surf. Sci.* **615**, 80 (2013)
91. J. Velev, R.F. Sabirianov, S.S. Jaswal, E.Y. Tsymbal, *Phys. Rev. Lett.* **94**, 127203 (2005)
92. D. Jacob, J. Fernández-Rossier, J.J. Palacios, *Phys. Rev. B* **77**, 165412 (2008)
93. G. Autès, C. Barreteau, D. Spanjaard, M.C. Desjonquères, *Phys. Rev. B* **77**(15), 155437 (2008)
94. A. Smogunov, A. Dal Corso, E. Tosatti, *Phys. Rev. B* **78**, 014423 (2008)
95. M. Häfner, J.K. Viljas, J.C. Cuevas, *Phys. Rev. B* **79**, 140410 (2009)
96. M. Viret, M. Gabureac, F. Ott, C. Fermon, C. Barreteau, G. Autes, R. Guirado-Lopez, *Eur. Phys. J. B* **51**(1), 1 (2006)
97. A. Sokolov, C. Zhang, E.Y. Tsymbal, J. Redepenning, B. Doudin, *Nat. Nanotechnol.* **2**(3), 171 (2007)
98. S. Egle, C. Bacca, H. Pernau, M. Huefner, D. Hinzke, U. Nowak, E. Scheer, *Phys. Rev. B* **81**, 134402 (2010)
99. B. Doudin, M. Viret, *J. Phys.: Condens. Matter* **20**(8), 083201 (2008)
100. K.I. Bolotin, F. Kuemmeth, D.C. Ralph, *Phys. Rev. Lett.* **97**, 127202 (2006)
101. S.F. Shi, D.C. Ralph, *Nat. Nanotechnol.* **2**, 522 (2007)
102. J. Schöneberg, F. Otte, N. Nel, A. Weismann, Y. Mokrousov, J. Kröger, R. Berndt, S. Heinze, *Nano Lett.* **16**(2), 1450 (2016)
103. M. Bode, S. Heinze, A. Kubetzka, O. Pietzsch, X. Nie, G. Bihlmayer, S. Blügel, R. Wiesendanger, *Phys. Rev. Lett.* **89**, 237205 (2002)
104. N. Néel, S. Schröder, N. Ruppelt, P. Ferriani, J. Kröger, R. Berndt, S. Heinze, *Phys. Rev. Lett.* **110**, 037202 (2013)
105. S. Schröder, Ph.D. thesis, University of Kiel, 2013
106. H. Birk, M.J.M. de Jong, C. Schönenberger, *Phys. Rev. Lett.* **75**, 1610 (1995)
107. M. Herz, S. Bouvron, E. Cavar, M. Fonin, W. Belzig, E. Scheer, *Nanoscale* **5**, 9978 (2013)
108. U. Kemiktarak, T. Ndukum, K.C. Schwab, K.L. Ekinci, *Nature* **450**(7166), 85 (2007)
109. H.E. van den Brom, J.M. van Ruitenbeek, *Phys. Rev. Lett.* **82**, 1526 (1999)
110. M. Kumar, R. Avriller, A.L. Yeyati, J.M. van Ruitenbeek, *Phys. Rev. Lett.* **108**, 146602 (2012)
111. N.L. Schneider, G. Schull, R. Berndt, *Phys. Rev. Lett.* **105**, 026601 (2010)
112. W. Schottky, *Ann. Phys.* **362**, 541 (1918)
113. T. Martin, R. Landauer, *Phys. Rev. B* **45**, 1742 (1992)
114. S. Heinze, M. Bode, A. Kubetzka, O. Pietzsch, X. Nie, S. Blügel, R. Wiesendanger, *Science* **288**, 1805 (2000)
115. A. Burtzloff, A. Weismann, M. Brandbyge, R. Berndt, *Phys. Rev. Lett.* **114**, 016602 (2015)
116. A. Kumar, L. Saminadayar, D.C. Glatli, Y. Jin, B. Etienne, *Phys. Rev. Lett.* **76**, 2778 (1996)
117. G.B. Lesovik, *Sov. Phys. JETP Lett.* **49**, 592 (1989)
118. E. Scheer, N. Agrait, J.C. Cuevas, A.L. Yeyati, B. Ludoph, A. Martin-Rodero, G.R. Bollinger, J.M. van Ruitenbeek, C. Urbina, *Nature* **394**, 154 (1998)